



# Extent, duration and timing of the sea ice cover in Hornsund, Svalbard, from 2014–2023

Zuzanna M. Swirad<sup>1</sup>, A. Malin Johansson<sup>2</sup>, and Eirik Malnes<sup>3</sup>

<sup>1</sup>Institute of Geophysics, Polish Academy of Sciences, Warsaw, Poland

<sup>2</sup>Department of Physics and Technology, UiT The Arctic University of Norway, Tromsø, Norway

<sup>3</sup>NORCE Norwegian Research Centre AS, Oslo, Norway

**Correspondence:** Zuzanna M. Swirad (zswirad@igf.edu.pl)

Received: 3 November 2023 – Discussion started: 14 December 2023

Revised: 5 February 2024 – Accepted: 6 February 2024 – Published: 27 February 2024

**Abstract.** The Sentinel-1A/B synthetic aperture radar (SAR) imagery archive between 14 October 2014 and 29 June 2023 was used in combination with a segmentation algorithm to create a series of binary ice/open-water maps of Hornsund fjord, Svalbard, at 50 m resolution for nine seasons (2014/15 to 2022/23). The near-daily (1.57 d mean temporal resolution) maps were used to calculate sea ice coverage for the entire fjord and its parts, namely the main basin and three major bays: Burgerbukta, Brepollen and Samarinvågen. The average length of the sea ice season was 158 d (range: 105–246 d). Drift ice first arrived from the southwest between October and March, and the fast-ice onset was on average 24 d later. The fast ice typically disappeared in June, around 20 d after the last day with drift ice. The average sea ice coverage over the sea ice season was 41 % (range: 23 %–56 %), but it was lower in the main basin (27 %) compared to in the bays (63 %). Of the bays, Samarinvågen had the highest sea ice coverage (69 %), likely due to its narrow opening and its location in southern Hornsund protecting it from the incoming wind-generated waves. Seasonally, the highest sea ice coverage was observed in April for the entire fjord and the bays and in March for the main basin. The 2014/15, 2019/20 and 2021/22 seasons were characterised by the highest sea ice coverage, and these were also the seasons with the largest number of negative air temperature days in October–December. The 2019/20 season was characterised by the lowest mean daily and monthly air temperatures. We observed a remarkable interannual variability in the sea ice coverage, but on a nine-season scale we did not record any gradual trend of decreasing sea ice coverage. These high-resolution data can be used to, e.g. better understand the spatiotemporal trends in

the sea ice distribution in Hornsund, facilitate comparison between Svalbard fjords, and improve modelling of nearshore wind wave transformation and coastal erosion.

## 1 Introduction

Sea ice plays a key role in the climate by controlling heat, moisture, gas and light transfer between the ocean and the atmosphere. It impacts wildlife and human activities at high latitudes. It modifies the wave energy transfer and, consequently, protects polar coasts from wave-driven erosion. Fast ice directly precludes waves from entering the foreshore and backshore (Rodzik and Zagórski, 2009), while drift ice attenuates wave energy, mostly at higher frequencies (Barnhart et al., 2014; Nederhoff et al., 2022).

The Arctic annual mean sea ice extent decreased by 3.5 %–4.1 % per decade between 1979 and 2012 (IPCC, 2019). At the same time, the sea-ice-free season along the Arctic coastlines increased 1.5–3 times (Barnhart et al., 2014). In the Fram Strait, west of Svalbard, increasing dominance of Atlantic water over polar water elevated sea surface temperatures, contributing to an intensified melting of the sea ice transported in the East Greenland Current and to delayed in situ ice growth (de Steur et al., 2023). In Svalbard itself, despite the high interannual variability (Smith and Lydersen, 1991; Gerland and Renner, 2007), there is a general decline in sea ice extent and duration observed for various locations, including Hornsund, Isfjorden, Kongsfjorden and Rijpfjorden (Muckenhuber et al., 2016; Pavlova et al., 2019; Johansson et al., 2020). Svalbard-wide fast-ice decline rates

of  $100 \text{ km}^2 \text{ yr}^{-1}$  were observed for 1973–2018 (Urbański and Litwicka, 2022). Fjords in western Svalbard experienced accelerated reduction in sea ice extent in 2000–2016 compared to in 1980–2000 (Dahlke et al., 2020). Simulations suggest that in 2060–2069 the western fjords and the northern Barents Sea will experience further reduction in sea ice concentration, reflecting increasing sea surface temperatures (Hanssen-Bauer et al., 2019).

With decreasing extent and duration of the sea ice cover and increasing storminess, Arctic coasts are exposed to larger waves during extended time periods (Forbes, 2011; Overeem et al., 2011; Zagórski et al., 2015). This intensifies coastal flooding and erosion, posing a risk of damage to infrastructure (Casas-Prat and Wang, 2020). Therefore, it is critical to understand the seasonal patterns and longer-term (years to decades) trends in sea ice coverage on a local (fjord) scale to better model nearshore wind wave transformation and wave energy delivery to the shores and, consequently, more accurately assess coastal hazards and risks.

Satellite data have been used in sea ice mapping since 1979 (Parkinson and Cavalieri, 2008). Passive-microwave-derived sea ice products have the longest temporal record but lack the high spatial resolution offered by synthetic aperture radar (SAR) imagery. Since May 2007, the Norwegian Meteorological Institute has provided manually drawn ice charts for Monday–Friday for the Arctic Ocean, including Svalbard (<https://cryo.met.no/en/ice-service>, last access: 24 July 2023). These maps make use of SAR images (most recently from the ESA Sentinel-1 missions), in situ observations and wind estimates. Several daily sea ice concentration products based on satellite images or models are available from the National Snow and Ice Data Center (<https://nsidc.org/data>, last access: 24 July 2023), the Copernicus Marine Data Store (<https://data.marine.copernicus.eu/products>, last access: 24 July 2023), the EUMETSAT Data Store (<https://navigator.eumetsat.int/start>, last access: 24 July 2023), the Ifremer Wind and Wave Operation Center (Ardhuin, 2022), and the University of Bremen (Melsheimer and Spreen, 2019). There are variations between the products in the areas around Svalbard (Swirad et al., 2023a), and this reflects their inconsistencies at the marginal ice zone, i.e. at the vicinity of the sea ice edge (Andersen et al., 2007; Ozsoy-Cicek et al., 2017; Pang et al., 2018). This may be due to diverse sensitivity of algorithms to sea ice temperature, atmospheric effects and thin ice (Ivanova et al., 2015). In coastal areas, the products may yield errors related to mixed land and water surface within the sensor footprint (Cavalieri et al., 1999). The product resolution of 1 to 25 km is often too low to analyse details in seasonal and interannual changes along the coast.

We use the method developed by Johansson et al. (2020) to make near-daily binary ice/open-water maps of Hornsund fjord in southern Svalbard based on the full Sentinel-1A/B SAR archive over nine seasons (2014/15–2022/23). We describe spatial and temporal distribution in the sea ice coverage and combine the results with an earlier (1999/2000–

2013/14) study of Muckenhuber et al. (2016) to identify longer-term (24-year) trends.

## 2 Study area

Hornsund fjord is located in southwestern Spitsbergen, Svalbard. Its opening to the Greenland Sea in the west is  $\sim 12$  km wide and defined by Worcesterpynten (north) and Palffyodden (south). The fjord is  $\sim 30$  km long and can be divided into the main basin and secondary bays as indicated in Fig. 1b. The inner (eastern) part, Brepollen, is  $\sim 13$  km long and separated from the main basin of Hornsund by a  $\sim 2$  km wide opening between Treskelodden (north) and Meranpynten (south). Burgerbukta is an  $\sim 8$  km long bay in northern Hornsund delimited by Hyrneodden (east) and Brattpynten (west). It branches into Austre (eastern) and Vestre (western) Burgerbukta. In southern Hornsund, Samarinvågen is  $\sim 7$  km long and defined by Meranpynten (east) and Traunpynten (west) (Fig. 1; <https://toposvalbard.npolar.no/>, last access: 4 July 2023).

The average fjord depth is  $\sim 100$  m, but it reaches 200–250 m in the main basin. The circulation is anticlockwise with inflow from the southwest and outflow to the northwest, and the average tidal range is 0.75 m (Herman et al., 2019). The influence of the West Spitsbergen Current that carries warm Atlantic water from the south-southwest is limited by the strong influence of the Sørkapp Current that brings cold water masses from the Barents Sea (Fig. 1a). Annual along-fjord CTD measurements conducted in July 2001–2015 showed surface layer temperatures of  $3$ – $6$  °C outside the fjord and in the main basin and  $0$ – $3$  °C in Brepollen, where at a depth of  $> 75$ – $100$  m the temperature was negative (Promińska et al., 2018).

Sea ice in Hornsund is either transported into the fjord from eastern Svalbard with the cold Sørkapp Current (blue line in Fig. 1a) or formed in situ as fast ice (Kruszewski, 2011). The ice drifting into the fjord from the southwest typically first appears in November–December, while the in situ fast-ice onset is between November and March. The fjord is usually sea-ice-free by the middle or end of June (Muckenhuber et al., 2016).

For the seasons 2005/06–2011/12, hand-drawn maps of the sea ice extent, concentration and type (stage of development and morphology) were made based on observations from the slopes of Fugleberget and Arieammen and from the Isbjørnhamna shore (Fig. 1). These maps covered the main basin closest to the Polish Polar Station (PPS), showing seasonal and interannual variability in the sea ice conditions, with the lowest sea ice coverage in 2005/06 and 2011/12 (Styszyńska and Kowalczyk, 2007; Styszyńska and Rozwadowska, 2008; Styszyńska, 2009; Kruszewski, 2010, 2011, 2012, 2013). Muckenhuber et al. (2016) used satellite data to investigate the fjord-wide sea ice coverage over 15 seasons (1999/2000–2013/14). April was characterised by the

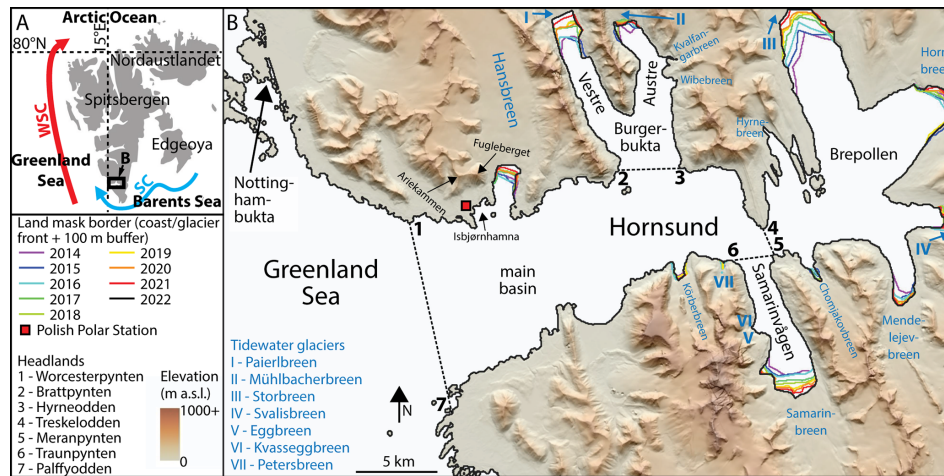


**Figure 1.** Study area: (a) Svalbard, (b) Hornsund. WSC – West Spitsbergen Current, SC – Sørkapp Current. DEM courtesy of the Polar Geospatial Center.

largest coverage of fast ice, averaging 42 % for all seasons and decreasing from an average of 53 % in the first six seasons to 35 % in the following nine seasons. The 2011/12 and 2013/14 seasons had the lowest fast-ice coverage, which at no point exceeded 40 %.

The average daily mean air temperature at the PPS in northern Hornsund was  $-3.7^{\circ}\text{C}$  for 1979–2018, with March being the coldest ( $-10.2^{\circ}\text{C}$ ) month and July the warmest ( $4.6^{\circ}\text{C}$ ) month. October to April had higher interannual air temperature variability compared to the more consistent May to September. There is a trend of increasing mean annual air temperature by  $1.14^{\circ}\text{C}$  per decade with the highest monthly increase of  $2.1\text{--}2.4^{\circ}\text{C}$  per decade in December, January and February (Wawrzyniak and Osuch, 2020).

Wind conditions recorded at the PPS are strongly influenced by the shape, topography and coastal location of the Hornsund fjord. In 1979–2018 the easterly winds dominated with a mean wind direction of  $124^{\circ}$  and an average wind speed of  $5.5\text{ m s}^{-1}$ , with a minimum mean monthly of  $4.0\text{ m s}^{-1}$  in July and a maximum mean monthly of  $7.1\text{ m s}^{-1}$  in February (Wawrzyniak and Osuch, 2020). Long oceanic swell and mixed swell/wind sea from the south-southwest and short, locally generated wind waves from the east determine wave conditions in the fjord. The mean significant wave height at the fjord opening is 1.2–1.3 m. It decreases to 0.25–0.43 m in the bays of the main basin and further in the inner sections of the fjord. Waves are higher and longer in northern Hornsund and in the winter months (Herman et al., 2019; Swirad et al., 2023c). Preliminary research suggests that sea ice present outside and inside the fjord attenuates wind wave energy, in particular at frequencies  $> 0.15\text{ Hz}$  (Swirad et al., 2023a).

The fjord is surrounded by 16 tidewater glaciers (Fig. 1b) which had a total cliff length of 34.7 km in 2010. The average retreat rate of the glacier front was  $70 \pm 15\text{ m yr}^{-1}$  in 2001–

2010 compared to  $45 \pm 15\text{ m yr}^{-1}$  for 128 glaciers in different parts of Svalbard. Because of the glacier front retreat, the fjord area increased from  $\sim 188\text{ km}^2$  in 1936 to  $\sim 303\text{ km}^2$  in 2010 (Błaszczuk et al., 2013). The average 2006–2015 freshwater input to the fjord was  $2517 \pm 82\text{ Mt yr}^{-1}$ , with contributions from glacier meltwater runoff (39 %), frontal ablation of tidewater glaciers (25 %), precipitation over land excluding snow (21 %), snowmelt (8 %) and precipitation over fjord (7 %) (Błaszczuk et al., 2019).

### 3 Methods

#### 3.1 Dataset and pre-processing

Sentinel-1A/B SAR data between 14 October 2014 and 29 June 2023 were used in this study, including 2508 Extra Wide (EW) and 459 Interferometric Wide (IW) scenes that fully covered the Hornsund fjord. Automated segmentation and classification were performed on 2486 (84 %) scenes that were of sufficient quality for processing and had both the HH and HV channels. If multiple scenes were available for the same date, only one was used, with preference given to (i) the one that required no/less manual edition, (ii) the IW scene and (iii) the EW scene with a mid-incidence angle range over Hornsund to ensure the best signal-to-noise ratio for both the HH and the HV channels. This resulted in the use of 2031 scenes, which constituted 68 % of all scenes and 82 % of the good-quality scenes. The temporal frequency averaged 1.57 d with a maximum gap of 12 d (no scenes on 17–28 June 2016) and a generally higher frequency between April 2016 and December 2021, when both Sentinel-1A and Sentinel-1B were operating.

We processed the data in the same way as Johansson et al. (2020), where the scenes were geocoded on a fixed grid using  $50 \times 50\text{ m}$  pixel spacing with the grid extent of  $X: 499\text{--}$

544 km and  $Y$ : 8531–8559 km of WGS 84, UTM zone 33N, using GSAR software (Larsen et al., 2006). For each scene, three GeoTIFF rasters were created with the radar backscatter sigma nought values (HH and HV separate) and the incidence angle.

### 3.2 Image segmentation

We used the segmentation algorithm developed by Cristea et al. (2020) and adapted to the Svalbard fjord environment by Johansson et al. (2020). The algorithm accounts for the surface-specific intensity decay rate with increased incidence angle, meaning that the different segments contain areas with the same physical structure, as was further shown by Cristea et al. (2022). For each new segment, the traditional expectation–maximisation algorithm is performed and a Pearson-style goodness-of-fit (GOF) test is carried out. If the test does not pass the GOF criterion, further splitting of the segments is carried out. Finally, Markov-random-field-based contextual smoothing and filtering are done to ensure simpler visual interpretation. For this study, we set the maximum number of segments deemed sufficient to separate ice from open water. In 90 % of the cases five segments were found to be suitable, and for the remaining 10 % a range of three to seven segments was used. The challenging cases were typically those with topography-driven varying wind characteristics across the scene and those where the SAR beam boundaries crossed the fjord (Johansson et al., 2020).

As a standard, both the HH and HV channels were used. The HV channel ensures good separation between open water and first-year ice (Zakhvatkina et al., 2017). However, because of the low signal-to-noise ratio, the HV channel does not necessarily improve the segmentation. At times, only one of the channels was used to ensure the best possible ice/open-water separation. During the segmentation, the images were multi-looked by  $3 \times 3$  and log-transformed (Johansson et al., 2020) and a land mask was used.

The land mask was created using the Norwegian Polar Institute's land shapefile (NPI, 2014). The mask was updated annually using the SAR scenes to account for glacier front retreats in the fjord. The scene from 1 July (or first available thereafter) was assumed to depict the furthest extent of the Hornsund glaciers after the front advance in spring (Błaszczuk et al., 2013). The 2014 mask was based on a RADARSAT-2 scene, and thereafter Sentinel-1 scenes were used. Each mask was applied to the following 1 July–30 June period. Finally, a 100 m buffer was added along the entire coast, with a larger buffer area of 3.3 km<sup>2</sup> of the shallow Notinghambukta delta (Fig. 1b) to exclude the tidal zone.

### 3.3 Ice/open-water classification and post-processing

The segmentation output was a GeoTIFF raster with approximately five discontinuous segments. The segments were manually classified as either “ice” or “open water” based on

user experience and assumptions of (i) low backscatter values of open water with calm wind conditions and higher values for ice and (ii) better separation of the two classes with the HV channel, which is less affected by wind-roughened surfaces (Johansson et al., 2020). The method does not allow for the separation of drift ice, fast ice and glacier ice. Figure 2 is an example of image segmentation and classification.

Of the 2031 scenes, 1432 (71 %) did not require manual editing after class assignment to the segments. However, 333 (16 %) scenes required minor manual changes consisting of adding/removing polygons to/from the ice class, and 266 (13 %) scenes required entirely manual ice polygon picking (without border drawing or polygon splitting) similar to that of Muckenhuber et al. (2016). Manual editing was preceded by the conversion of GeoTIFF rasters into polygons and followed by rasterisation. The classification resulted in near-daily binary maps of ice (1) and open water (0) available in the PANGAEA repository (Swirad et al., 2023b), together with a document containing details on the scenes and channels used, the number of segments and the level of manual editing.

The sea ice extent (m<sup>2</sup>) and coverage (%) were extracted for the entirety of Hornsund and separately for Burgerbukta, Brepollen, Samarnvågen and the main basin (as delimited in Fig. 1b) for the 2031 scenes (days). The time series is available as Table S1 in the Supplement. The annual onset and end of drift ice and fast ice were defined visually from the raw scenes and the binary maps. For the drift ice, these were dates of the first and the last presence of ice drifting within the fjord delimited by Worcesterpynten and Palffyodden, excluding short-term episodes in summer and autumn. For the fast ice, the onset (or end) was the date on which the ice area with clear and stable edges was first (or last) visible in the inner parts of the fjord over the following (or preceding) days. Notably, very thin, freshly formed ice would not be visible. Analyses were performed on an annual basis starting in September (lowest sea ice coverage after Johansson et al., 2020) and ending in August. For instance, the 2014/15 season spanned 1 September 2014–31 August 2015. The sea ice season, however, started with the first arrival of drift ice from the southwest on 29 December 2014 and ended on the last day with fast ice on 7 July 2015.

### 3.4 Validation

The method was validated in Johansson et al. (2020) by comparing the classification results and the location of the fast-ice edge tracked with a handheld GPS and by comparing manually drawn maps from Zeppelin Mountain above Ny-Ålesund. Since the same pre-processing, segmentation algorithm set-up and classification method were used, we also consider these results valid for our study in Hornsund. Additionally, we manually traced the fast-ice edge in 20 Sentinel-2 optical images that were acquired on the same days as Sentinel-1 SAR scenes, had cloud cover below 10 % and had



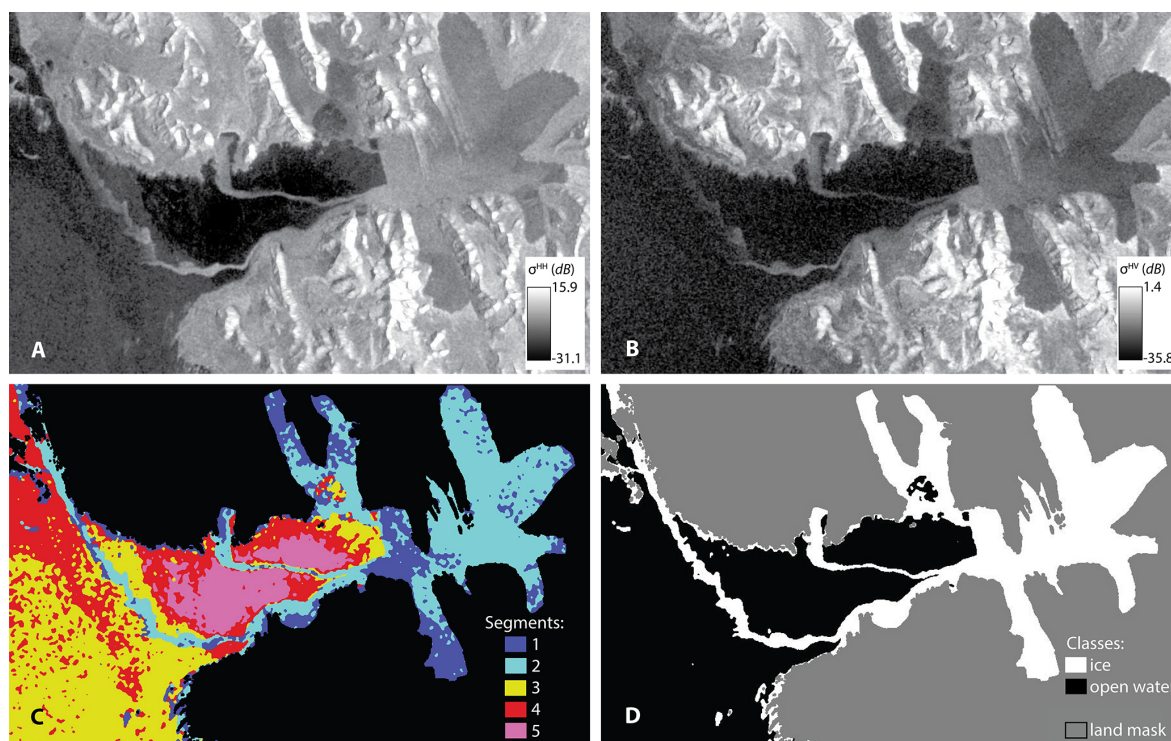


**Figure 2.** Illustration of the segmentation and classification of the S1\_EWM\_20220417\_054210\_DES\_037 scene: (a) HH backscatter intensity, (b) HV backscatter intensity, (c) segmented image with five discontinuous segments and the land mask (black), (d) classified image.

an unambiguous fast-ice edge position without adjacent drift ice. We converted classified sea ice polygons into lines and extracted the fast-ice edge. To measure the distance between lines of uneven nod distributions, we resampled both lines at 5 m (0.1 px) spacing and applied the “Distance to Nearest Hub (Points)” tool in QGIS. In total, we compared 299.23 km of fast-ice edge (59 866 points). The mean distance varied from  $43 \pm 31$  to  $131 \pm 177$  m (average 80 m), equivalent to  $0.85 \pm 0.62$  to  $2.62 \pm 3.53$  px (average 1.59 px). Table S2 in the Supplement contains details on the validation.

### 3.5 Additional datasets

Muckenhuber et al. (2016) provided a time series of open-water, fast-ice and drift ice extent ( $\text{m}^2$ ) in Hornsund for 1381 satellite images between 1 March 2000 and 8 June 2014. To enable direct comparison with our results, we calculated sea ice coverage (%) as  $(\text{fast-ice extent} + \text{drift ice extent})/\text{total extent} \times 100\%$ .

Continuous meteorological data from the PPS are available at <https://monitoring-hornsund.igf.edu.pl/> (last access: 5 July 2023). The mean daily air temperature is derived from 3-hourly automated measurements with Vaisala HMP45D and HMP155 probes at 2 m a.g.l. ( $\sim 12$  m a.s.l.) in the vicinity of the main buildings of the PPS, ca. 200 m from the shore. Seawater temperature measurements are performed daily at 12:00 UTC on the shore next to the PPS boathouse using an

ELMETRON PT-401 thermometer. The readings are representative of the top 50 cm layer. Data gaps, mostly in winter months, are caused by the presence of ice or strong winds.

## 4 Results

Binary ice/open-water maps at 50 m resolution were made for the period 14 October 2014 to 29 June 2023 at an average frequency of 1.57 d (Swirad et al., 2023b). The ice coverage varied in space and time during the inspected nine seasons (Fig. 3).

The first day of drifting sea ice entering the fjord from the southwest was between October and March. The fast-ice onset was on average 24 d later, between December and March. The last day of drift ice was in May or June and occurred on average 20 d before the end of the fast-ice season in June, except for 2014/15 (July) and 2015/16 (May). The length of the entire sea ice season (drift ice and fast ice) averaged 158 d, ranging from 105 (2015/16) to 246 d (2019/20). The length of the fast-ice season was on average 134 d, ranging from 61 to 195 d in 2015/16 and 2019/20, respectively (Table 1).

The average sea ice coverage in Hornsund during the entire sea ice season was 41 %, ranging from 23 % in 2015/16 to 56 % in 2019/20 (Table 1; Fig. A1). The coverage was lower in the main basin (average 27 %, range 6.1 %–41 %) compared to in the bays (average 63 %, range 41 %–74 %), and,

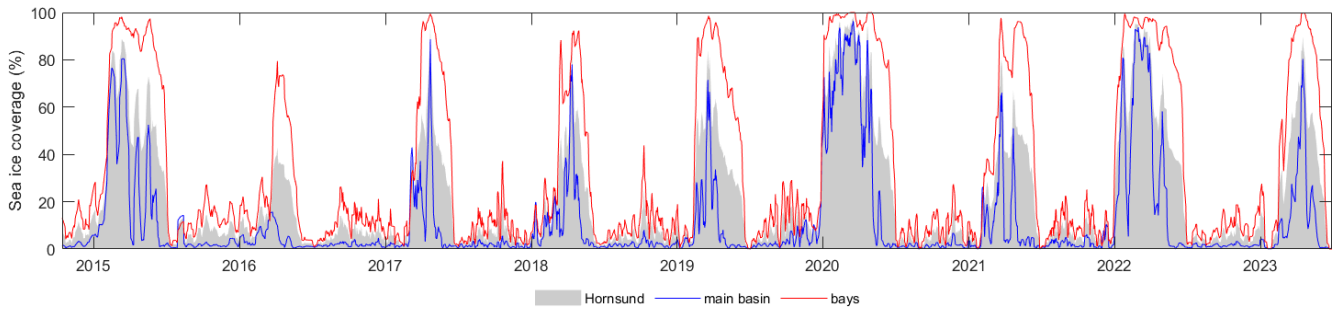


**Figure 3.** Time series of sea ice coverage in Hornsund from 2014–2023 derived for the whole fjord (shadow), the main basin (blue line) and the bays (red line) smoothed over five scenes. The term “bays” refers to Burgerbukta, Brepollen and Samarinvågen, as delimited in Fig. 1.

**Table 1.** Timing and duration of sea ice coverage in Hornsund from 2014–2023 and the mean coverage in the entire fjord and separately in the main basin and the bays (Burgerbukta, Brepollen and Samarinvågen, as delimited in Fig. 1).

Season	First day with drift ice	Fast-ice onset	Last day with drift ice	Fast-ice end	Length of sea ice season (days)	Length of fast ice season (days)	Mean sea ice coverage (%)					
							Entire sea ice season			Fast-ice season		
							Hornsund	Main basin	Bays	Hornsund	Main basin	Bays
2014/15	29 Dec	27 Jan	13 Jun	7 Jul	191	162	49	27	74	54	30	81
2015/16	15 Feb	30 Mar	26 May	29 May	105	61	23	6.1	41	28	3.6	55
2016/17	1 Mar	7 Mar	18 May	18 Jun	110	104	41	18	66	43	18	70
2017/18	30 Dec	29 Jan	23 May	4 Jun	157	127	29	15	43	34	18	51
2018/19	25 Jan	12 Feb	3 Jun	18 Jun	145	127	40	14	67	45	16	76
2019/20	28 Oct	18 Dec	26 May	29 Jun	246	195	56	41	72	67	49	87
2020/21	2 Feb	4 Feb	8 Jun	24 Jun	143	141	39	14	64	39	14	65
2021/22	3 Dec	28 Dec	23 May	22 Jun	202	177	52	34	70	62	41	85
2022/23	11 Feb	21 Feb	24 May	12 Jun	122	112	45	19	71	48	21	77
Average	11 Jan	4 Feb	27 May	17 Jun	158	134	41	21	63	47	23	72

of the three bays, Burgerbukta had the lowest ice coverage (average 50 %) compared to Brepollen (67 %) and Samarinvågen (69 %) (Fig. 4). The sea ice coverage during the fast-ice season was on average 6.5 % higher than during the entire sea ice season and shows the same spatial and temporal trends (Table 1).

The highest sea ice coverage in Hornsund occurred in April with an average of 58 %, followed by March (56 %), May (40 %) and February (36 %). In the bays, the maximum coverage was in April (88 %), May (75 %), March (73 %) and February (47 %). In the main basin, the highest average coverage characterised March (41 %), April (31 %) and February (26 %) (Figs. A2–A7). At no time during the entire study period did the mean monthly sea ice coverage in the main basin exceed that of the bays. The 2014/15, 2019/20 and 2021/22 seasons were characterised by an early (January–February) increase in sea ice coverage by 58 %–66 % in the entire fjord and by 63 %–80 % in the bays. In the 2019/20 season the coverage remained relatively high for both the main basin and the bays, with the latter experiencing a mean monthly coverage of > 90 % over 5 consecutive months (Fig. 5).

There was a secondary coverage peak around October that reached up to 20 %–40 % for specific days (Fig. 3). The ice coverage in summer and autumn was typically related to tide-

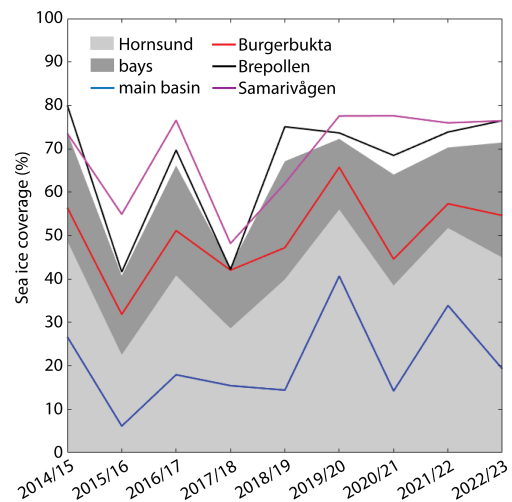


**Figure 4.** Average sea ice coverage during the entire sea ice season (from the first day of drift ice to the last day of fast ice) for Hornsund and its parts from 2014–2023. The term “bays” refers to Burgerbukta, Brepollen and Samarinvågen, as delimited in Fig. 1.

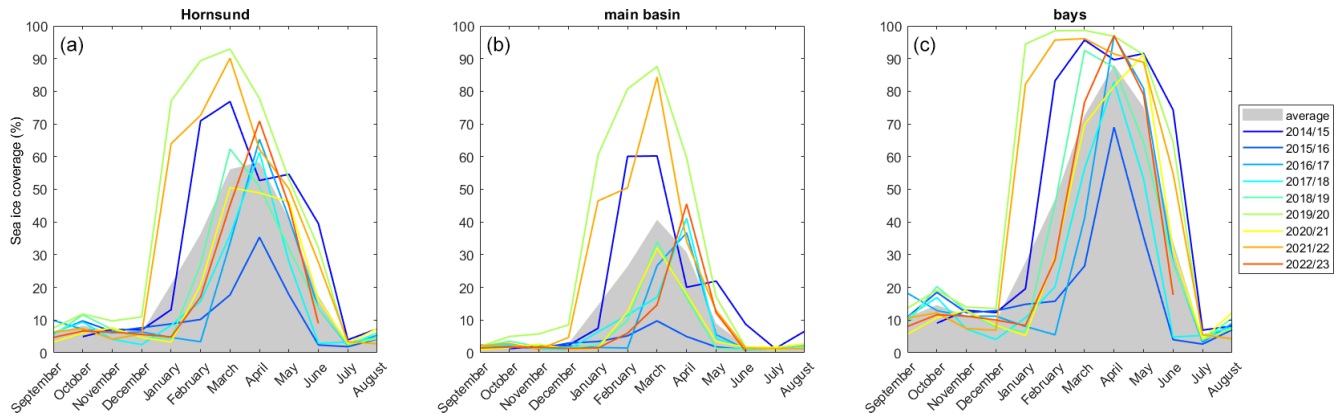


**Figure 5.** Distribution of the mean monthly sea ice coverage (%) in Hornsund from 2014–2023 over (a) the entire fjord, (b) the main basin and (c) the bays (Burgerbukta, Brepollen and Samarinvågen, as delimited in Fig. 1).

water glacier calving, though occasionally its increase was caused by drift ice from the southwest, such as on 7 August 2015.

Overall, an early onset of drift ice and fast ice and a long sea ice season and high sea ice coverage of both the main basin and the bays characterised 2014/15, 2019/20 and 2021/22. The 2015/16 season was short, with late drift ice and fast-ice onset and low sea ice coverage. Other short seasons were 2016/17 and 2022/23, and that of low coverage was 2017/18 (Figs. 3–5; Table 1).

Figures 6 and 7 show changes in the sea ice coverage in Hornsund for 24 seasons. They are a compilation of the present study and that of Muckenhuber et al. (2016). In the period of 1 March 2000–14 November 2005 only optical images were used, which made ice detection during the dark season (November–February) impossible. From 15 November 2005, Envisat ASAR (150 m resolution) scenes facilitated more regular temporal coverage throughout the year, though the resolution might have affected the retrieved ice coverage. From 1 November 2011, near-daily RADARSAT-2 (50 m resolution) data were used throughout the sea ice season (Fig. 6). In earlier years (1999/2000–2010/11) the sea ice season was generally longer, extending to the second half of June to the beginning of July, and the onset was relatively early (November–December; identifiable only since the SAR imagery became available) (Fig. 6). Over the 24-year period, the 2005/06, 2013/14 and 2015/16 seasons were characterised by the lowest sea ice coverage, which never exceeded 80%. The 2011/12 season was short with inconsistent coverage on a short-term (days/weeks) scale. Seasons with high sea ice coverage were 2007/08–2010/11, 2012/13 (Muckenhuber et al., 2016), 2014/15, 2019/20 and 2021/22 (Fig. 7).

The lowest mean daily and monthly air temperatures occurred in 2019/20 (Fig. 8; Table 2), which was the longest analysed sea ice season with the highest mean sea ice coverage (Table 1). The seasons with below-average mean monthly air temperatures were 2022/23, 2014/15, 2017/18

and 2021/22, two of which (2014/15 and 2021/22) were also “icy”. The three seasons with the highest sea ice coverage (2014/15, 2019/20 and 2021/22) overlapped with the years of the highest number of negative air temperature days in October–December but did not stand out in terms of later (January–June) air temperature or the number of positive air temperature days in the preceding year. The 2015/16 season, which had the lowest sea ice duration and coverage, had an exceptionally high minimal mean monthly air temperature ( $-5.5^{\circ}\text{C}$ ), and, similarly to the 2017/18 season, which also had low sea ice coverage, it had an early onset of positive air temperatures in spring. The 2016/17 season, with its short sea ice duration, had the highest number of positive air temperatures in the preceding year and, consequently, the latest onset of negative air temperatures in autumn. The 2022/23 season also had short sea ice duration but did not stand out in terms of the air temperature variables included here. The longest negative seawater temperature period was in the 2014/15 season with its high sea ice coverage, and the shortest was in the 2016/17 season with its short sea ice duration, but there are no clear trends for other seasons (Table 2).

## 5 Discussion

### 5.1 Consideration of the method

The segmentation algorithm of Cristea et al. (2020) facilitated efficient mapping of sea ice in the Hornsund fjord. The method differed from that of Muckenhuber et al. (2016), as it usually (87%) did not require manual classification of single ice polygons but rather required classifying a small number (three to seven) of discontinuous segments into ice or open water, which is likely quicker and more accurate.

We consistently used Sentinel-1A/B SAR data, where both the HH and HV channels were used in 1858 scenes, the HH only in 83 scenes, and the HV only in 90 scenes. We observed that rough water conditions often resulted in ambiguous seg-

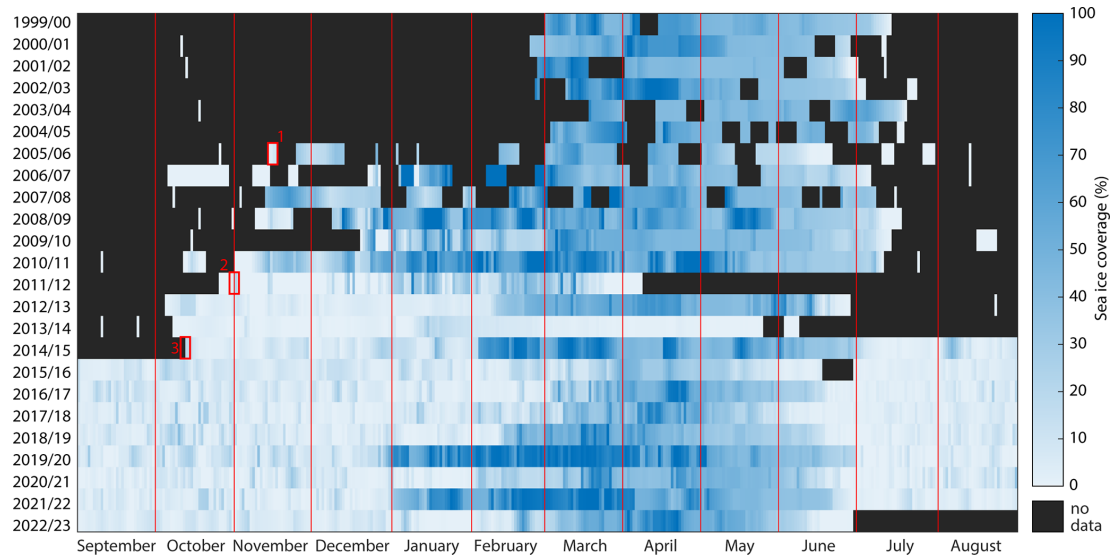


**Figure 6.** Sea ice coverage in Hornsund from 2000–2023. Data from 1 March 2000–8 June 2014 were adapted from Muckenhuber et al. (2016), of which results from 14 October 2014–29 June 2023 were processed in this study. The x axis represents days of the season starting 1 September (as in Johansson et al., 2020), and the y axis represents seasons. Linear interpolation over a maximum of 7 d was applied. First SAR scenes used: 1 – Envisat ASAR (15 November 2005), 2 – RADARSAT-2 (1 November 2011), 3 – Sentinel-1A/B (14 October 2014).

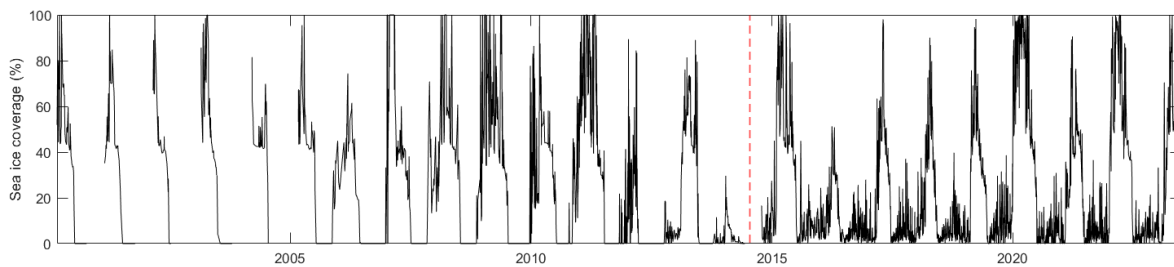


**Figure 7.** Sea ice coverage in Hornsund from 2000–2023. The dashed red line separates the data adapted from Muckenhuber et al. (2016) and those from the present study. Note that different processing resulted in inclusion of glacier ice in our study, unlike in Muckenhuber et al. (2016), and that there are data gaps in the dark season (November–February) prior to the 2005/06 season caused by the use of optical imagery only.

mentation in the HH channel, whereas the HV channel provided improved segmentation, and the problem was persistent in the Envisat ASAR data where only HH data were available. Thin and wet ice detection was sometimes hampered, particularly in the HV channel, due to the lower power return. The HV channel also suffers from beam boundaries created by the TOPS mode of Sentinel-1, which may make interpretation challenging.

The erroneous detection of ice may be related to radar shadowing and layover caused by topography; inclusion of shallow areas during low tide (though this was addressed by masking 100 m at the coast with a larger mask in Nottinghambukta); atmospheric, wind and ocean wave effects; and temporal objects such as ships (Jones, 2023). On the other hand, the erroneous lack of detection may occur when sea ice is thin and wet and difficult to separate from open water

(Johansson et al., 2020). We addressed such situations during the manual editing of 29 % of the scenes, though not all errors could be removed.

## 5.2 Types of ice

The semi-automated classification approach did not allow for separating drift ice, fast ice and glacier ice, as the backscatter signatures are largely similar. We observed the lowest ice coverage in July, followed by a gradual increase with a peak around October (Fig. 8). We interpret this as tidewater glacier calving activity, a finding consistent with Błaszczuk et al. (2013), who recorded the most intense calving in August–November. However, caution should be taken when using our dataset for glacier ice analysis, as (i) brash ice, growlers and bergy bits may only be detected when grouped;



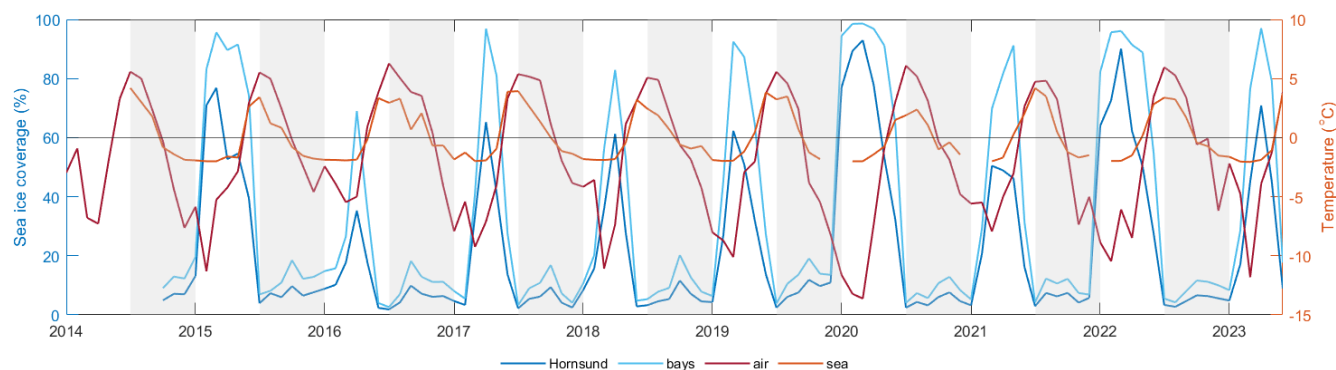


**Figure 8.** Mean monthly sea ice coverage in Hornsund and the bays (Burgerbukta, Brepollen and Samarinvågen, as delimited in Fig. 1) and air and seawater temperatures from 2014–2023. The meteorological data were downloaded from <https://monitoring-hornsund.igf.edu.pl/> (last access: 5 July 2023).

**Table 2.** Air and seawater temperature characteristics in Hornsund from 2014–2023. The meteorological data were downloaded from <https://monitoring-hornsund.igf.edu.pl/> (last access: 5 July 2023).

Season	Minimum daily air temperature (°C)	Minimum monthly air temperature (°C)	Number of days with negative air temperature in Sep–Dec	Number of days with negative air temperature in Jan–Mar	Number of days with negative air temperature in Apr–Jun	Number of days with positive air temperature in the preceding year	Negative sea water temperature timing	Negative sea water temperature duration (length in days)
2014/15	−19.3	−11.3	77	80	52	168	23 Sep–3 Jun	254
2015/16	−16.1	−5.5	61	75	37	170	24 Sep–22 May	242
2016/17	−16.6	−9.2	37	79	57	212	26 Oct–24 May	211
2017/18	−15.0	−11.1	58	79	35	170	6 Oct–22 May	229
2018/19	−20.8	−10.1	65	88	41	186	11 Sep–14 May	246
2019/20	−24.4	−13.6	87	90	41	147	10 Oct–6 Jun	241
2020/21	−18.2	−7.9	60	83	53	173	4 Oct–23 May	232
2021/22	−20.1	−10.5	78	83	50	149	30 Sep–15 May	228
2022/23	−19.8	−11.8	61	77	43	169	12 Oct–30 May	231
Average	−19.4	−10.1	65	82	45	172	3 Oct–25 May	235

(ii) during the sea ice period the glacier ice is blended with the sea ice; and (iii) the 100 m coastal buffer of the land mask filters out glacier ice accumulated in bays and glacier forefields.

We visually established the onset and end of the presence of drift ice and fast ice. The drift ice originates from two sources: it is brought from the southwest by the Sørkapp Current or broken off from the fast ice formed in situ. Drifting sea ice is therefore more common in the main basin of Hornsund than in the bays. The differences in sea ice timing and coverage in the main basin and in the bays (Fig. 5) agree with the observations of drift ice and fast ice, respectively, by Muckenhuber et al. (2016), e.g. on the earlier onset of drift ice and the peak timing of the two types. The bays create the best locations for fast-ice formation because of the shelter from waves and wind. Of the three considered bays, Burgerbukta had the lowest (and most changing on a seasonal scale) sea ice coverage, which might be related to the higher wind wave energy in northern Hornsund, which is directly related to the long oceanic swell direction (Herman et al., 2019; Swirad et al., 2023c). In Brepollen, the narrow opening and the presence of a sill restrict water exchange with the main basin, and relatively cold and low-salinity water per-

sists throughout the year (Promińska et al., 2018). Good conditions for fast-ice formation and persistence in Samarinvågen may be related to its calm water (south shore of Hornsund), its low incoming wind wave energy, and its narrow and elongated shape.

### 5.3 Seasonal trends

Insight into seasonal patterns of sea ice conditions was provided by visual observations and ice situation sketching during seven consecutive seasons (2005/06–2011/12) in the vicinity of the PPS (Styszyńska and Kowalczyk, 2007; Styszyńska and Rozwadowska, 2008; Styszyńska, 2009; Kruszewski, 2010, 2011, 2012, 2013). The observations suggest that the main basin experiences higher variability in sea ice extent and concentration compared to the Burgerbukta, Brepollen and Samarinvågen bays (visible also in Fig. 3), which is related to the direct impact of instantaneous wind conditions and the ice situation outside Hornsund on the situation in the main basin (Kruszewski, 2012). The pack ice drifting from the southwest in the Sørkapp Current ranges from grey ice (10–15 cm thick) to thick first-year ice (< 2 m) (Styszyńska and Kowalczyk, 2007; Styszyńska, 2009). The



presence of drift ice in Hornsund is dynamic on a daily to weekly scale, but in 2007/08 it remained in the fjord for 9 consecutive weeks (Styszyńska, 2009). Dominating strong easterly winds can make drift ice concentration in the main basin of Hornsund lower than that of the open Greenland Sea (Kruszewski, 2011). The short-term variability in sea ice coverage in Hornsund is visible for the 24 seasons in Fig. 7.

Fast ice forms in the major bays and occasionally along less indented sections of the coasts. It is often broken by strong winds and waves and drifts towards the main basin. Because of temperature variability, particularly in autumn and early winter, ice formation may start two or three times, and it is interchanged with ice melting and/or breaking at periods of higher air temperatures and/or stronger winds. At its maximum in 2010/11 the fast ice covered most of the main basin, while in 2011/12 it only extended across a portion of Brepollen (Kruszewski, 2012, 2013). The short-term fluctuations in sea ice coverage are clearly visible in Fig. 3.

Glacier ice is present in the fjord year-round in the form of brash ice, growlers, bergy bits and occasionally icebergs (Kruszewski, 2010). It decreases the temperature and salinity of the surface water along the shore of Isbjørnhamna. In autumn, between glacier ice, new sea ice forms in situ: frazil ice, grease ice, shuga, nilas, grey ice, and (later) grey-white ice and pancake ice. Along the coast of the main basin, an ice foot forms as a combination of glacier and sea ice and freezing of swash, splashes and snow. It remains at the sea–land border until June–July, protecting the beach from erosion and redistribution of the material by waves (Rodzik and Zagórski, 2009; Zagórski et al., 2015).

#### 5.4 Interannual trends

The presence of drift ice in Hornsund depends on winds, currents and tides (Kruszewski, 2010). On the contrary, the in situ sea ice formation depends on the intensity of heat release to the atmosphere, which increases with lower temperatures and higher wind speeds (Styszyńska and Kowalczyk, 2007) that control the thickness of the seawater surface mixed layer (Promińska et al., 2018). However, on a 9-year scale, we do not observe an expected decrease in fast-ice coverage (Figs. 3 and 5) as a reflection of the air warming trend observed at the PPS (Warzyniak and Osuch, 2020). The reason for this may be that the number of seasons studied here is too low for such long-term trends. Similarly, for a 14-season (1974/75–1987/88) period, Smith and Lydersen (1991) observed a considerable interannual variability in Hornsund fast-ice duration ranging from 0 to 166 d prior to 1 April but not a gradual trend.

To expand the analysis and identify longer-term trends, we combined our study with that of Muckenhuber et al. (2016), which covered 15 preceding sea ice seasons. Three differences in datasets and/or methods need to be considered when interpreting the merged time series. Firstly, prior to the 2005/06 season only optical images were used, so it is impos-

sible to analyse the ice season start and length and the winter-time coverage and its variability. Secondly, manual polygon classification into drift ice and fast ice by Muckenhuber et al. (2016) at the cost of efficiency has potential to better link ice types with environmental factors deemed to control ice conditions, e.g. fast ice with temperature and drift ice with wind and currents. Finally, the binary classification applied here does not allow filtering out glacier ice (see Fig. 7).

Notably, Muckenhuber et al. (2016) stated that sea ice declined during the 15-season time series, with 2 seasons of low sea ice coverage (2011/12 and 2013/14) occurring at the end of the analysed period. In our study, however, in the second half of the monitoring period, two seasons (2019/20 and 2021/22) were characterised by the highest mean sea ice coverage (Table 1), while 2011/12 and 2013/14 remain the seasons of the lowest sea ice coverage in Hornsund in the 21st century (Fig. 6). In addition, 2012 was the year of the lowest pan-Arctic sea ice extent (<https://nsidc.org/arcticseaicenews/2023/09/arctic-sea-ice-minimum-at-sixth/>, last access: 26 September 2023). The annual fast-ice extent analysis across Svalbard by Urbański and Litwicka (2022) showed that there is a longer-term (1973–2018) trend of decreasing total fast-ice extent by an average of  $100 \text{ km}^2 \text{ yr}^{-1}$ , which resulted in the halving of fast ice over this  $\sim 45$ -year period. The modelling suggested that air temperature (freezing degree days) has a 60 % influence on the interannual extent and duration of the fast ice (Urbański and Litwicka, 2022). For the Fram Strait, de Steur et al. (2023) found a direct relationship between seawater temperature and sea ice concentration, but the relationship is still to be determined for the Svalbard fjords.

There is, however, an overlap of higher air temperatures and lower sea ice coverage with lower air temperatures and higher sea ice coverage. Warm seasons with little sea ice were 2005/06, 2011/12, 2013/14, 2015/16 and 2016/17. Cold seasons with a lot of sea ice were 2002/03, 2003/04, 2007/08, 2008/09, 2009/10, 2010/11, 2012/13, 2014/15, 2019/20 and 2021/22 (Figs. 6–8; Styszyńska, 2009; Kruszewski, 2012, 2013; Muckenhuber et al., 2016; Promińska et al., 2018). This pattern reflects the Svalbard-wide fast-ice extent (Urbański and Litwicka, 2022).

For 14 field monitoring seasons in Kongsfjorden (2002/03–2015/16), Pavlova et al. (2019) observed an abrupt change between high sea ice coverage in the first 3 seasons and reduced sea ice extent and duration in the following 11 seasons. The minimum was reached in 2011/12, while in 2009/10 and 2010/11 the sea ice coverage was high (Pavlova et al., 2019). Similar abrupt change starting in 2005/06 was observed by Muckenhuber et al. (2016) for Isfjorden with the lowest sea ice coverage in 2011/12 and 2013/14. Based on SAR images, Johansson et al. (2020) documented low sea ice coverage in Kongsfjorden in consecutive seasons 2005/06–2007/08 and 2011/12–2018/19 and in Rijpfjorden in 2011/12, 2015/16 and 2017/18. These findings generally agree with the situation in Hornsund (Fig. 7). We suggest that

the differences may be related to the local conditions, such as currents, winds and fjord shape. Due to the interference of the Sørkapp Current with the West Spitsbergen Current, the hydrographic conditions in Hornsund may differ considerably from those of more northern fjords (Promińska et al., 2018).

### 5.5 Further considerations

We did not find relationships between seawater temperature at the foreshore of Isbjørnhamna and sea ice coverage (Table 2). Because of the in-person character of the water temperature measurement, the data are missing for 34 % of the period 1 January 2014–30 June 2023. Days when no measurement was taken were characterised by the presence of ice and/or strong winds, and a note of the conditions was usually made in the report. When fast ice was present, the water surface temperature could be assumed to be below the saltwater freezing point of  $-1.78^{\circ}\text{C}$ , while, when the sea/glacier ice cover was discontinuous, it was probably close to the freezing point. Therefore, we generally treated no data as negative temperature (see negative temperature timing and length in Table 2 despite the lack of data for a considerable part of the winter). Kruszewski (2011) observed that the foreshore seawater temperature was higher when the waves were smaller and during the low tide. Continuous mooring (see e.g. De Rovere et al., 2022 for Kongsfjorden) would allow measurements from a depth of  $\sim 20\text{--}50\text{ m}$  that would be relevant to sea ice but independent from instantaneous weather/surface conditions. Such an approach was used by de Steur et al. (2023), who found a correlation between upper-layer (55 m) water temperature and sea ice concentration in the western Fram Strait. For this study, we only extracted the timing and length of negative surface water temperatures, parameters likely independent from inaccuracies related to the measurement strategy and circumstances.

The interactions between sea ice and glaciers are multifaceted and still not fully explored. We have discussed the contribution of glacier ice to the fjord ice and its impact on sea surface temperature and local in situ sea ice formation. However, the presence of sea ice can also impact glacier dynamics by decreasing glacier front calving. In Hornsund, Pętlicki et al. (2015) observed that pack ice restricted wave action at the front of the tidewater glacier Hansbreen in 2011, limiting notch development around the waterline and, consequently, leading to failure of the overhanging ice.

Our method does not allow the determination of drift ice concentration at a 50 m resolution, an important parameter in modelling wind wave transformation. For instance, the Simulating WAVes Nearshore (SWAN) model takes sea ice concentration as an input to account for dissipation of wave energy caused by the presence of ice (Rodgers, 2019). High-concentration drift ice on the Greenland Sea attenuates energy of long oceanic swell and mixed swell/wind sea, while in situ ice precludes wind wave generation over the eastern parts of the fjord (Styszyńska and Rozwadowska, 2008). Ig-

norning the sea ice in nearshore wave modelling may cause an overestimation of significant wave height, an underestimation of wave period and an overall overestimation of the total wave energy (Herman et al., 2019; Swirad et al., 2023a). Norwegian Meteorological Institute ice charts and various sea ice concentration products provide this information; however, their resolution is lower than that of nearshore wave models. We suggest down-scaling our binary maps to the resolution of a wave model, which would allow a calculation of the sea ice concentration on a lower-resolution scale under the assumption of 100 % concentration in the “ice” pixels and 0 % concentration in the “open-water” pixels. In the future, splitting the sea ice mapped here into smaller, more homogeneous segments with field calibration and a classification method similar to Lohse et al. (2019, 2020) could be tested.

The ice situation in Hornsund impacts transportation and landing and is particularly troublesome during the PPS crew exchange in June–July when cargo is loaded and unloaded in Isbjørnhamna. In July 2008, a 52 km wide belt of drift ice of varied concentration made it difficult for the cargo ship to reach the PPS area (Styszyńska, 2009). In 2004 no hydrographic measurements could be made during the annual *R/V Oceania* cruise in July because of the dense sea ice cover in the fjord (Promińska et al., 2018). On the other hand, the ice protects the beach from erosion and, consequently, the PPS boathouse from damage. A later onset of the sea ice season may allow early winter storms to enter coastal zones, increasing the hazard of flooding and erosion (Zagórski et al., 2015). High-spatial- and temporal-resolution studies, such as this one, may help better predict the probability of sea ice conditions at specific times of the year.

## 6 Conclusions

Sentinel-1A/B SAR imagery between 16 October 2014 and 29 June 2023 was used in combination with a segmentation algorithm and a classification to create near-daily binary ice/open-water maps at 50 m resolution for Hornsund fjord, southwestern Svalbard (Swirad et al., 2023b). The maps were used to identify spatial and temporal patterns in the sea ice coverage, with the intention to be used as sea ice input into nearshore wind wave transformation and coastal erosion models.

Sea ice in Hornsund has a dual origin: it arrives from the southwest in the cold Sørkapp Current or is formed in situ. Over the analysed nine seasons, 2014/15 to 2022/23, the average length of the sea ice season was 158 d, ranging from 105 to 246 d. Drift ice first appeared between October and March, preceding the onset of fast ice by  $\sim 24\text{ d}$ . The end of the sea ice season was related to the removal of fast ice from the inner parts of the fjord in June (July in 2014/15 and May in 2015/16),  $\sim 20\text{ d}$  after the last drift ice presence in the fjord.

The average total sea ice coverage over the sea ice season was 41 %, ranging between 23 % and 56 %. It was lower in the main basin (27 %) and higher in the inner bays, Burgerbukta, Brepollen and Samarinvågen (63 %). Of the bays, Burgerbukta had the lowest (50 %) and Samarinvågen had the highest (69 %) average sea ice coverage. We suggest that this is related to the differences in wave energy delivered to the northern vs. the southern shores of Hornsund with long oceanic swell and mixed swell/wind sea from the south-southwest affecting the northern shores, which contributes to sea ice breaking at the relatively wide opening of Burgerbukta.

The highest sea ice coverage characterised March for the main basin and April for the bays. Because of the arrival of drift ice from the southwest and a preferential persistence of fast ice in the calmer-water bays, we suggest that this timing reflects the peak occurrence of drift ice (March) and fast ice (April). There is a secondary peak around October, which we interpret as glacier ice from calving of tidewater glaciers.

Our data show high interannual variability. The highest sea ice coverage characterised 2014/15, 2019/20 and 2021/22, seasons that also had the largest number of negative air temperature days in October–December. The “iciest”, 2019/20, was characterised by the lowest mean daily and monthly air temperatures. On the nine-season scale we were not able to identify any gradual trend of decreasing sea ice coverage.

Combining our results with the previous study of Muckenhuber et al. (2016) gives a full picture of sea ice coverage in Hornsund in the first 24 years of the 21st century. The lowest sea ice coverage characterised the 2011/12 and 2013/14 seasons. Generally, shorter sea ice seasons and lower sea ice coverage coincided with higher air temperatures, while long seasons and high sea ice coverage occurred in cold years.

The results further the understanding of the sea ice extent, duration and timing in a high-Arctic fjord environment and facilitate between-site comparison of changing sea ice conditions in Svalbard. The binary ice/open-water maps can be further used to improve nearshore wind wave transformation modelling and risk assessment for the coastal zone.

## Appendix A: Extended figures

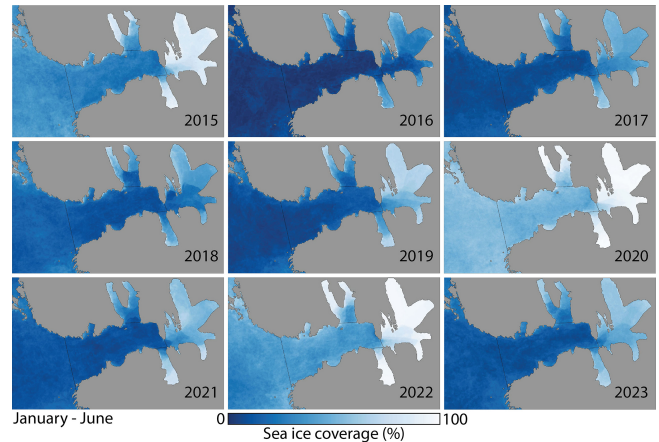


**Figure A1.** Mean sea ice coverage in Hornsund in January–June 2015–2023.

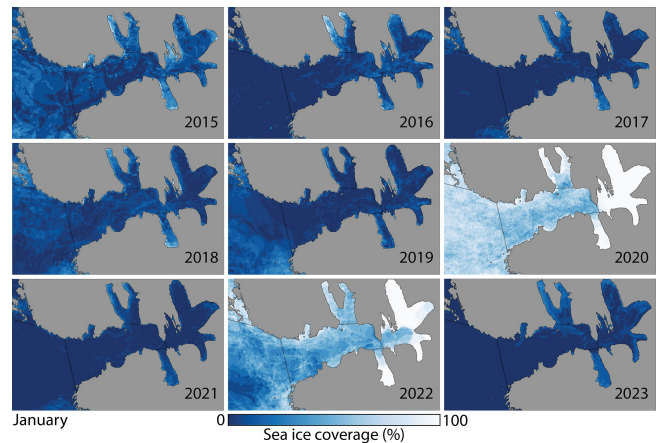


**Figure A2.** Mean sea ice coverage in Hornsund in January 2015–2023.

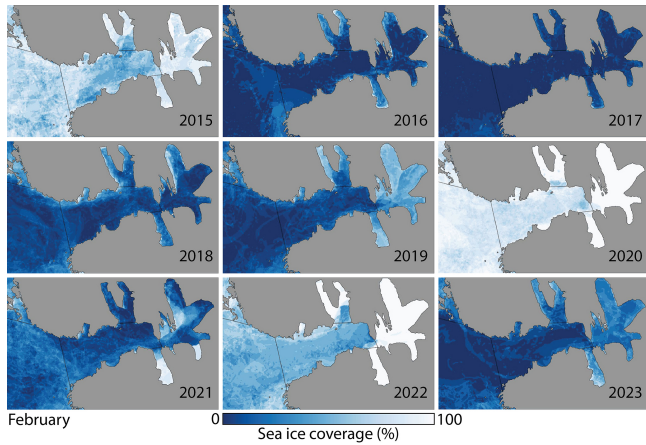


**Figure A3.** Mean sea ice coverage in Hornsund in February 2015–2023.

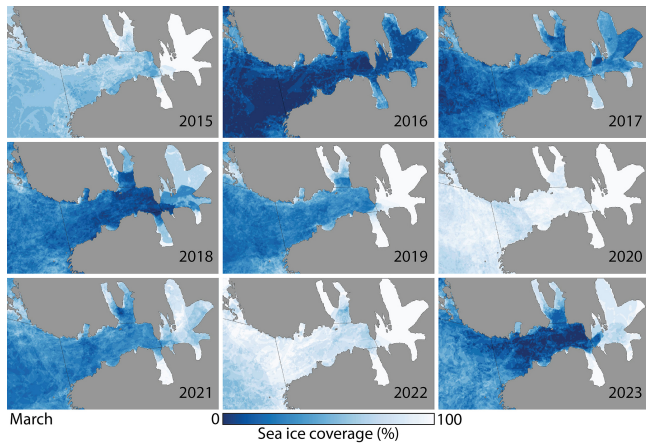


**Figure A4.** Mean sea ice coverage in Hornsund in March 2015–2023.

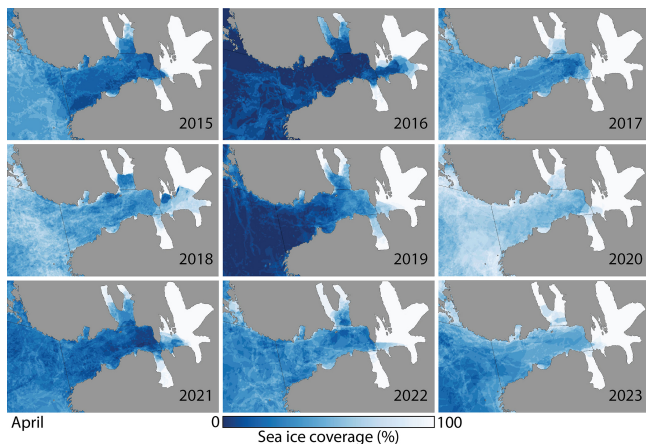


**Figure A5.** Mean sea ice coverage in Hornsund in April 2015–2023.

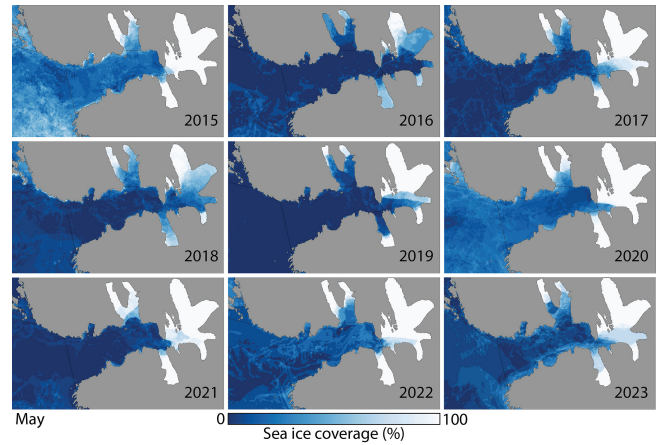


**Figure A6.** Mean sea ice coverage in Hornsund in May 2015–2023.

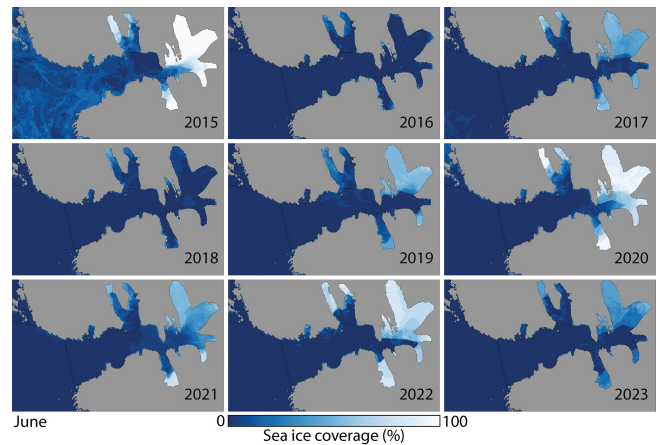


**Figure A7.** Mean sea ice coverage in Hornsund in June 2015–2023.

*Data availability.* Binary ice/open-water maps are available in the PANGAEA repository (<https://doi.org/10.1594/PANGAEA.963167>; Swirad et al., 2023b). Table S1 in the Supplement is the summary of sea ice extent (m<sup>2</sup>) and coverage (%) for Hornsund and its parts (as delimited in Fig. 1b) based on the binary maps.

*Supplement.* The supplement related to this article is available online at: <https://doi.org/10.5194/tc-18-895-2024-supplement>.

*Author contributions.* ZMS conceptualised the study, secured the funding and compiled the environmental data. EM pre-processed the SAR scenes. AMJ developed the image processing method. ZMS processed and analysed the data with the help of AMJ. All authors interpreted the results and wrote the article.

*Competing interests.* The contact author has declared that none of the authors has any competing interests.

*Disclaimer.* Publisher's note: Copernicus Publications remains neutral with regard to jurisdictional claims made in the text, published maps, institutional affiliations, or any other geographical representation in this paper. While Copernicus Publications makes every effort to include appropriate place names, the final responsibility lies with the authors.

*Acknowledgements.* We thank Anthony Doulgeris for the discussion on the segmentation algorithm and the Polar Polish Station crew for maintaining the meteorological monitoring. We acknowledge the European Union's Earth observation programme, Copernicus, which freely provides the Sentinel-1 and Sentinel-2 data (<https://scihub.copernicus.eu>, last access: 24 July 2023).

*Financial support.* This study was funded by the National Science Centre of Poland (SONATINA 5 grant no. 2021/40/C/ST10/00146). A. Malin Johansson was supported by CIRFA and the Research Council of Norway under grant no. 237906. Eirik Malnes was partly supported by the Research Council of Norway under the project "Svalbard Integrated Arctic Earth Observing System – Infrastructure development of the Norwegian node" (SIOS-InfraNor project no. 269927).

*Review statement.* This paper was edited by John Yackel and reviewed by two anonymous referees.

## References

- Andersen, S., Tonboe, R., Kaleschke, L., Heygster, G., and Pedersen, L. T.: Intercomparison of passive microwave sea ice concentration retrievals over the high-concentration Arctic sea ice, *J. Geophys. Res.*, 112, C08004, <https://doi.org/10.1029/2006JC003543>, 2007.
- Ardhuin, F.: IWWOC Arctic Sea Ice Backscatter Gridded Level 3 Composite from SCAT onboard CFOSAT, Ifremer [data set], <https://doi.org/10.12770/6d58c023-6fe5-4cae-937b-479166a6f517>, 2022.
- Barnhart, K. R., Overeem, I., and Anderson, R. S.: The effect of changing sea ice on the physical vulnerability of Arctic coasts, *The Cryosphere*, 8, 1777–1799, <https://doi.org/10.5194/tc-8-1777-2014>, 2014.
- Błaszczak, M., Jania, J. A., and Kolondra, L.: Fluctuations of tide-water glaciers in Hornsund fjord (southern Svalbard) since the beginning of the 20th century, *Pol. Polar Research*, 34, 327–352, 2013.
- Błaszczak, M., Ignatiuk, D., Uszczyk, A., Cielecka-Nowak, K., Grabiec, M., Jania, J. A., Moskalik, M., and Walczowski, W.: Freshwater input to the Arctic fjord Hornsund (Svalbard), *Polar Res.*, 38, 3506, <https://doi.org/10.33265/polar.v38.3506>, 2019.
- Casas-Prat, M. and Wang, X. L.: Projections of extreme ocean waves in the Arctic and potential implications for coastal inundation and erosion, *J. Geophys. Res.-Oceans*, 125, e2019JC015745, <https://doi.org/10.1029/2019JC015745>, 2020.
- Cavalieri, D. J., Parkinson, C. L., Gloersen, P., Comiso, J. C. and Zwally, H. J.: Deriving long-term time series of sea ice cover from satellite passive-microwave multisensor data sets, *J. Geophys. Res.*, 104, 15803–15814, <https://doi.org/10.1029/1999JC900081>, 1999.
- Cristea, A., van Houtte, J., and Doulgeris, A. P.: Integrating Incidence Angle Dependencies Into the Clustering-Based Segmentation of SAR Images, *IEEE J. Sel. Top. Appl.*, 13, 2925–2939, <https://doi.org/10.1109/JSTARS.2020.2993067>, 2020.
- Cristea, A., Johansson, A. M., Doulgeris, A. P., and Brekke, C.: Automatic Detection of Low-Backscatter Targets in the Arctic Using Wide Swath Sentinel-1 Imagery, *IEEE J. Sel. Top. Appl.*, 15, 8870–8883, <https://doi.org/10.1109/JSTARS.2022.3214069>, 2022.
- Dahlke, S., Hughes, N., Wagner, P., Gerland, S., Wawrzyniak, T., Ivanov, B., and Maturilli, M.: The observed recent surface air temperature development across Svalbard and concurring footprints in local sea ice cover, *Int. J. Climatol.*, 40, 5246–5265, <https://doi.org/10.1002/joc.6517>, 2020.
- De Rovere, F., Langone, L., Schroeder, K., Misericocchi, S., Giglio, F., Aliani S., and Chiggiato, J.: Water masses variability in inner Kongsfjorden (Svalbard) during 2010–2020, *Front. Mar. Sci.*, 9, 741075, <https://doi.org/10.3389/FMARS.2022.741075>, 2022.
- de Steur, L., Sumata, H., Divine, D. V., Granskog, M. A., and Pavlova O.: Upper ocean warming and sea ice reduction in the East Greenland Current from 2003 to 2019, *Commun. Earth Environ.*, 4, 261, <https://doi.org/10.1038/s43247-023-00913-3>, 2023.
- Forbes, D.: State of the Arctic Coast 2010 – Scientific Review and Outlook, Tech. Rep., International Arctic Science Committee, Land-ocean Interactions in the Coastal Zone, Arctic Monitoring and Assessment Programme, International Permafrost Association, Helmholtz-Zentrum, Geesthacht, Germany, 178 pp., <http://arcticcoasts.org> (last access: 18 July 2023), 2011.
- Gerland, S. and Renner, A. H. H.: Sea-ice mass-balance monitoring in an Arctic fjord, *Ann. Glaciol.*, 46, 435–442, <https://doi.org/10.3189/172756407782871215>, 2007.
- Hanssen-Bauer, I., Førland, E. J., Hisdal, H., Mayer, S., Sandø, A. B., Sorteberg, A., Adakudlu, M., Andresen, J., Bakke, J., Beldring, S., Benestad, R., Bilt, W., Bogen, J., Borstad, C., Breili, K., Breivik, Ø., Børsheim, K. Y., Christiansen, H. H., Dobler, A., Engeset, R., Frauenfelder, R., Gerland, S., Gjelten, H. M., Gunderson, J., Isaksen, K., Jaedicke, C., Kierulf, H., Kohler, J., Li, H., Lutz, J., Melvold, K., Mezghani, A., Nilsen, F., Nilsen, I. B., Nilsen, J. E. Ø., Pavlova, O., Ravndal, O., Risebrobakken, B., Saloranta, T., Sandven, S., Schuler, T. V., Simpson, M. J. R., Skogen, M., Smedsrud, L. H., Sund, M., Vikhamar-Schuler, D., Westermann, S., and Wong, W. K.: Climate in Svalbard 2100, 1/2019, <https://www.miljodirektoratet.no/globalassets/publikasjoner/M1242/M1242.pdf> (last access: 1 September 2023), 2019.
- Herman, A., Wojtysiak, K., and Moskalik, M.: Wind wave variability in Hornsund fjord, west Spitsbergen, *Estuar. Coast. Shelf S.*, 217, 96–109, <https://doi.org/10.1016/j.ecss.2018.11.001>, 2019.
- IPCC: The Ocean and Cryosphere in a Changing Climate, International Panel on Climate Change, <https://www.ipcc.ch/srocc/home> (last access: 24 July 2023), 2019.
- Ivanova, N., Pedersen, L. T., Tonboe, R. T., Kern, S., Heygster, G., Lavergne, T., Sørensen, A., Saldo, R., Dybkjær, G., Brucker, L., and Shokr, M.: Inter-comparison and evaluation of sea ice algorithms: towards further identification of challenges and optimal approach using passive microwave observa-



- tions, *The Cryosphere*, 9, 1797–1817, <https://doi.org/10.5194/tc-9-1797-2015>, 2015.
- Johansson, A. M., Malnes, E., Gerland, S., Cristea, A., Doulgeris, A. P., Divine, D. V., Pavlova, O., and Lauknes, T. R.: Consistent ice and open water classification combining historical synthetic aperture radar satellite images from ERS-1/2, Envisat ASAR, RADARSAT-2 and Sentinel-1A/B, *Ann. Glaciol.*, 61, 40–50, <https://doi.org/10.1017/aog.2019.52>, 2020.
- Jones, C. E.: An automated algorithm for calculating the ocean contrast in support of oil spill response, *Mar. Pollut. Bull.*, 191, 114952, <https://doi.org/10.1016/j.marpolbul.2023.114952>, 2023.
- Kruszewski, G.: Ice conditions in Hornsund (Spitsbergen) during winter season 2008–2009, *Problemy Klimatologii Polarnej*, 20, 187–196, 2010 (in Polish).
- Kruszewski, G.: Ice conditions in Hornsund during winter season 2009–2010 (SW Spitsbergen), *Problemy Klimatologii Polarnej*, 21, 229–239, 2011 (in Polish).
- Kruszewski, G.: Ice conditions in Hornsund and adjacent waters (Spitsbergen) during winter season 2010–2011, *Problemy Klimatologii Polarnej*, 22, 69–82, 2012 (in Polish).
- Kruszewski, G.: Ice conditions in Hornsund and adjacent waters (Spitsbergen) during winter season 2011–2012, *Problemy Klimatologii Polarnej*, 23, 169–179, 2013 (in Polish).
- Larsen, Y., Engen, G., Lauknes, T., Malnes, E., and Høgda, K.: A generic differential interferometric SAR processing system, with applications to land subsidence and snow-water equivalent retrieval, *Fringe 2005 Workshop*, 610, ISBN 92-9092-921-9, 2006.
- Lohse, J., Doulgeris, A. P., and Dierking, W.: An optimal decision-tree design strategy and its application to sea ice classification from SAR imagery, *Remote Sens.*, 11, 1574, <https://doi.org/10.3390/rs11131574>, 2019.
- Lohse, J., Doulgeris, A. P., and Dierking, W.: Mapping sea-ice types from Sentinel-1 considering the surface-type dependent effect of incidence angle, *Ann. Glaciol.*, 61, 260–270, <https://doi.org/10.1017/aog.2020.45>, 2020.
- Melsheimer, C. and Spreen, G.: AMSR2 ASI sea ice concentration data, Arctic, version 5.4 (NetCDF) (July 2012–December 2019), PANGAEA [data set], <https://doi.org/10.1594/PANGAEA.898399>, 2019.
- Muckenhuber, S., Nilsen, F., Korosov, A., and Sandven, S.: Sea ice cover in Isfjorden and Hornsund, Svalbard (2000–2014) from remote sensing data, *The Cryosphere*, 10, 149–158, <https://doi.org/10.5194/tc-10-149-2016>, 2016.
- NPI: Kartdata Svalbard 1:100 000 (S100 Kartdata)/Map Data, Norwegian Polar Institute [data set], <https://doi.org/10.21334/npolar.2014.645336c7>, 2014.
- Nederhoff, K., Erikson, L., Engelstad, A., Bieniek, P., and Kasper, J.: The effect of changing sea ice on wave climate trends along Alaska's central Beaufort Sea coast, *The Cryosphere*, 16, 1609–1629, <https://doi.org/10.5194/tc-16-1609-2022>, 2022.
- Overeem, I., Anderson, R. S., Wobus, C. W., Clow, G. D., Urban, F. E., and Matell, N.: Sea ice loss enhances wave action at the Arctic coast, *Geophys. Res. Lett.*, 38, L17503, <https://doi.org/10.1029/2011GL048681>, 2011.
- Ozsoy-Cicek, B., Ackley, S., Worby, A., Xie, H., and Lieser, J.: Antarctic sea-ice extents and concentrations: Comparison of satellite and ship measurements from International Polar Year cruises, *Ann. Glaciol.*, 52, 318–326, <https://doi.org/10.3189/172756411795931877>, 2011.
- Pang, X., Pu, J., Zhao, X., Ji, Q., Qu, M., and Cheng, Z.: Comparison between AMSR2 Sea Ice Concentration Products and Pseudo-Ship Observations of the Arctic and Antarctic Sea Ice Edge on Cloud-Free Days, *Remote Sens.*, 10, 317, <https://doi.org/10.3390/rs10020317>, 2018.
- Parkinson, C. L. and Cavalieri, D. J.: Arctic sea ice variability and trends, 1979–2006, *J. Geophys. Res.*, 113, C07003, <https://doi.org/10.1029/2007JC004558>, 2008.
- Pavlova, O., Gerland, S., and Hop, H.: Changes in sea ice extent and thickness in Kongsfjorden, Svalbard (2003–2016), in: *The Ecosystem of Kongsfjorden, Svalbard*, edited by: Hop, H. and Wiencke, C., *Advances in Polar Ecology*, 2, Springer, Cham, 105–136, [https://doi.org/10.1007/978-3-319-46425-1\\_4](https://doi.org/10.1007/978-3-319-46425-1_4), 2019.
- Petlicki, M., Ciepły, M., Jania, J. A., Promińska, A., and Kinnard, C.: Calving of tidewater glacier driven by melting at the waterline, *J. Glaciol.*, 61, 851–863, <https://doi.org/10.3189/2015JoG15J062>, 2015.
- Promińska, A., Falck, E., and Walczowski, W.: Interannual variability in hydrography and water mass distribution in Hornsund, an Arctic fjord in Svalbard, *Polar Res.*, 37, 1495546, <https://doi.org/10.1080/17518369.2018.1495546>, 2018.
- Rodgers, W. E.: Implementation of Sea Ice in the Wave Model SWAN, Naval Research Laboratory, Washington, DC, USA, 32 pp., <https://apps.dtic.mil/sti/trecms/pdf/AD1073081.pdf> (last access: 26 February 2024), 2019.
- Rodzik, J. and Zagórski, P.: Shore ice and its influence on development of shores of the southwestern Spitsbergen, *Oceanol. Hydrobiol. S.*, 38, 163–180, 2009.
- Smith, T. G. and Lydersen, C.: Availability of suitable land-fast ice and predation as factors limiting ringed seal populations, *Phoca hispida*, in Svalbard, *Polar Res.*, 10, 585–594, <https://doi.org/10.3402/polar.v10i2.6769>, 1991.
- Styszyńska, A.: Ice conditions in Hornsund and its foreshore (south-west Spitsbergen) during winter season 2007/08, *Problemy Klimatologii Polarnej*, 19, 247–267, 2009 (in Polish).
- Styszyńska, A. and Kowalczyk, M.: Ice conditions in Hornsund and its foreshore (south-west Spitsbergen) during winter season 2005/06, *Problemy Klimatologii Polarnej*, 17, 147–158, 2007 (in Polish).
- Styszyńska, A. and Rozwadowska, A.: Ice conditions in Hornsund and its foreshore (south-west Spitsbergen) during winter season 2006/07, *Problemy Klimatologii Polarnej*, 18, 141–160, 2008 (in Polish).
- Swirad, Z. M., Herman, A., Johansson, A. M., Rees, W. G., and Moskalik, M.: Incorporating sea ice into a nearshore wind wave transformation model (Hornsund, Svalbard), *Figshare*, <https://doi.org/10.6084/m9.figshare.22302658.v1>, 2023a.
- Swirad, Z. M., Johansson, A. M., and Malnes, E.: Ice distribution in Hornsund fjord, Svalbard from Sentinel-1A/B (2014–2023), PANGAEA [data set], <https://doi.org/10.1594/PANGAEA.963167>, 2023b.
- Swirad, Z. M., Moskalik, M., and Herman, A.: Wind wave and ater level dataset for Hornsund, Svalbard (2013–2021), *Earth Syst. Sci. Data*, 15, 2623–2633, <https://doi.org/10.5194/essd-15-2623-2023>, 2023c.
- Urbański, J. A. and Litwicka, D.: The decline of Svalbard land-fast sea ice extent as a result of climate change, *Oceanologia*, 64, 535–545, <https://doi.org/10.1016/j.oceano.2022.03.008>, 2022.

- Wawrzyniak, T. and Osuch, M.: A 40-year High Arctic climatological dataset of the Polish Polar Station Hornsund (SW Spitsbergen, Svalbard), *Earth Syst. Sci. Data*, 12, 805–815, <https://doi.org/10.5194/essd-12-805-2020>, 2020.
- Zagórski, P., Rodzik, J., Moskalik, M., Strzelecki, M. C., Lim, M., Błaszczak, M., Promińska, A., Kruszewski, G., Styszyńska, A., and Malczewski, A.: Multidecadal (1960–2011) shoreline changes in Isbjørnhamna (Hornsund, Svalbard), *Pol. Polar Res.*, 36, 369–390, 2015.
- Zakhvatkina, N., Korosov, A., Muckenhuber, S., Sandven, S., and Babiker, M.: Operational algorithm for ice–water classification on dual-polarized RADARSAT-2 images, *The Cryosphere*, 11, 33–46, <https://doi.org/10.5194/tc-11-33-2017>, 2017.